ACCSCIENCE PUBLISHING

International Journal of Bioprinting

RESEARCH ARTICLE

3D bioprinting of patient-derived cholangiocarcinoma organoids in a decellularized liver matrix-based bioink for drug testing

Qiumei Yan[1†], Wenqi Hu[2,3†], Jiashu Wang[2,3], Luping Lü[2,3], Zhuge Yang[2,3], Zixuan Pan[2,3], Yonggang Guo[2,3], Jie Liu[2,3], Huanhuan Chen[2,3], Di Wu[2,3,4], Qijun Du[2,3,5], Haijie Hu[6], Bin Lai[2,3], Yabao Liu[2,3], Guohua Wu[7,8*], Xiongwen Chen[1*], and Bangchuan Hu[9*]

[1]Tianjin Key Laboratory on Technologies Enabling Development of Clinical Therapeutics and Diagnostics, Department of Biopharmaceuticals, School of Pharmacy, Tianjin Medical University, Tianjin, China

[2]College of Biomedical Engineering, Sichuan University, Chengdu, Sichuan, China

[3]National Engineering Research Center for Biomaterials, Sichuan University, Chengdu, Sichuan, China

[4]Department of Respiratory and Critical Care Medicine, West China Hospital, Sichuan University, Chengdu, Sichuan, China

[5]State Key Laboratory of Respiratory Health and Multimorbidity, West China Hospital, Sichuan University, Chengdu, Sichuan, China

[6]Division of Biliary Surgery, Department of General Surgery, West China Hospital, Sichuan University, Chengdu, Sichuan, China

[7]Luoyang Key Laboratory of Clinical Multiomics and Translational Medicine, The First Affiliated Hospital and College of Clinical Medicine, Henan University of Science and Technology, Luoyang, Henan, China

[8]Henan Key Laboratory of Rare Diseases, Endocrinology and Metabolism Center, The First Affiliated Hospital and College of Clinical Medicine, Henan University of Science and Technology, Luoyang, Henan, China

[9]Emergency and Critical Care Center, ICU, Zhejiang Provincial People's Hospital, Hangzhou Medical College, Hangzhou, Zhejiang, China

[†]*These authors contributed equally to this work.*

***Corresponding authors:**
Guohua Wu
(wuguohua@zju.edu.cn)
Xiongwen Chen
(Xiongwenchen@tmu.edu.cn)
Bangchuan Hu
(hubangchuanicu@163.com)

Citation: Yan Q, Hu W, Wang J, *et al.* 3D bioprinting of patient-derived cholangiocarcinoma organoids in a decellularized liver matrix-based bioink for drug testing. *Int J Bioprint.* 2026;12(3):026200188.
doi: 10.36922/IJB026200188

Received: May 13, 2026

Revised: June 11, 2026

Accepted: June 15, 2026

Published online: June 15, 2026

Abstract

Cholangiocarcinoma (CCA) shows marked interpatient heterogeneity in chemotherapy response, highlighting the need for physiologically relevant, standardized, and reproducible *in vitro* models for individualized drug screening. However, Matrigel-based organoid models lack hepatobiliary extracellular matrix cues, and many bioprinting strategies rely on dissociated or fragmented organoids, disrupting native architecture and spatial organization. To address these limitations, we developed a composite bioink for direct bioprinting of patient-derived CCA organoid (CCAO) fragments that retained multicellular organization, enabling standardized culture, imaging, and drug-response evaluation. Although decellularized liver matrix (DLM) was used to reconstruct the tissue-specific microenvironment, its weak gelation, poor mechanical properties, and limited printability restricted its application. Tris(2,2′-bipyridyl)ruthenium(II)/sodium persulfate (Ru/SPS) and gelatin methacryloyl (GelMA) were introduced to improve photocrosslinking, mechanical

support, and printability. DLM retained key components of the hepatic extracellular matrix, including collagen, fibronectin, laminin, and glycosaminoglycans. With GelMA and Ru/SPS, the bioink achieved rapid visible-light crosslinking (405 nm, 50 seconds), tunable mechanical properties, and good extrusion-printing compatibility. Among the tested formulations, the DLM-Ru/SPS:GelMA (4:1) group showed the best balance of printability, transparency, and organoid-compatible microstructure. Using this optimized bioink, organoid fragments were patterned and reassembled into viable spheroids that retained key CCA features and maintained high viability (>80%). The platform also enabled reproducible assessment of drug response, demonstrating dose-dependent cisplatin sensitivity and enhanced cytotoxicity with cisplatin–gemcitabine treatment. In summary, this study established a DLM-based direct bioprinting platform for CCAOs and a standardized system for individualized therapeutic evaluation.

Keywords: Three-dimensional bioprinting; Bioink; Cholangiocarcinoma; Decellularized liver matrix; Patient-derived organoids; Drug screening

1. Introduction

Cholangiocarcinoma (CCA) is a highly aggressive malignancy arising from the biliary epithelium and is characterized by marked molecular and histological heterogeneity[1-3], leading to a poor prognosis and a five-year survival rate of less than 20%[4,5]. Because most patients are diagnosed at an advanced stage and are no longer eligible for curative resection, systemic therapy remains the main treatment option for unresectable or metastatic disease.[6,7] However, the standard first-line regimen of gemcitabine plus cisplatin offers only limited clinical benefit, and therapeutic resistance frequently occurs.[8,9] In addition, patients without actionable molecular alterations or those who fail targeted therapy are often treated empirically in clinical practice, yet interpatient heterogeneity in genetic background, tumor differentiation, and microenvironment results in highly variable drug responses.[7,10,11] Consequently, empirical treatment may expose patients to ineffective regimens, unnecessary toxicity, and delayed access to more effective therapies. Therefore, there is an urgent need for patient-derived *in vitro* drug screening models that can accurately predict individual therapeutic responses and facilitate precision treatment decisions.

Current drug screening platforms mainly include two-dimensional (2D) cell culture, animal models, and patient-derived organoids. Although 2D culture systems are easy to operate[12], cost-effective, and suitable for high-throughput screening, they fail to recapitulate the three-dimensional (3D) architecture of tumors[13,14], the extracellular matrix (ECM) microenvironment, and complex cell–cell and cell–matrix interactions.[14,15] Animal models can partially reflect *in vivo* drug responses, but their use is limited by long establishment times, high costs, low throughput, and interspecies differences.[16,17] In contrast, patient-derived organoids better preserve the histological, genetic, and functional characteristics of the original tumors and have emerged as valuable tools for precision oncology and individualized drug screening.[18-20] Nevertheless, most existing organoid bioprinting strategies rely on dissociated single cells, cell aggregates, or fragmented organoids, which require mechanical or enzymatic disruption before printing and subsequent reassembly after printing. This process compromises the original cellular composition and spatial architecture of organoids, prolongs model construction, and limits control over organoid formation, distribution, and morphology.[21,22] As a result, conventional organoid bioprinting approaches often suffer from poor reproducibility and limited spatial precision. By contrast, direct bioprinting of intact patient-derived organoids may better preserve their multicellular architecture and biological characteristics while enabling standardized fabrication and spatial control. However, studies on the direct bioprinting of intact patient-derived CCA organoids (CCAOs) remain scarce, largely because of the lack of suitable bioinks.

An ideal bioink for CCAO printing should provide not only favorable printability, shape fidelity, and mechanical stability, but also a tissue-specific bioactive microenvironment that supports long-term survival, phenotypic maintenance, and drug-response assessment.[23,24] Conventional organoid culture typically relies on Matrigel embedding[25,26]; however, as a generic matrix, Matrigel lacks the tissue-specific ECM cues required to faithfully recapitulate the microenvironment associated with tumor initiation, progression, invasion, metastasis,

and drug response.[27,28] In contrast, decellularized ECM (dECM) retains tissue-specific structural and biochemical features, making it a promising material for constructing physiologically relevant organoid microenvironments.[29,30] Because CCA originates from the hepatobiliary system, a decellularized liver matrix (DLM) may better mimic the native niche of CCA cells and thereby improve the physiological relevance and predictive value of drug screening.[31,32] However, the poor gelation capacity and weak mechanical properties of DLM remain major barriers to its direct application in bioprinting.[33,34]

To overcome these limitations, we previously conducted a series of studies to improve the printability of dECM-based materials. In our DLM–gelatin methacryloyl (GelMA) sandwich-structured tumor-chip platform, DLM effectively preserved key ECM components, including collagen, fibronectin, laminin, and glycosaminoglycans, while GelMA crosslinking under 405 nm light for 25 seconds yielded a hydrogel with a Young's modulus of 5.69 kPa, demonstrating that material hybridization and optimized crosslinking can significantly improve the gelation and mechanical properties of DLM.[35-37] In addition, our studies on the decellularized kidney matrix–ruthenium/sodium persulfate (Ru/SPS) system showed that Ru/SPS enabled rapid gelation in approximately 40 seconds under 405 nm light, with improved gelation efficiency and shape fidelity.[37] Furthermore, in a stiffness-tunable hydrogel microfluidic chip for CCAOs, the introduction of GelMA and crosslinking with $CaCl_2$ enabled precise tuning of hydrogel stiffness to 2.9–13.31 kPa, and this tunable mechanical microenvironment was shown to regulate the hydrogel microfluidic chip for CCAOs' proliferation, differentiation, and drug sensitivity.[38] Collectively, these findings indicate that GelMA and photocrosslinking systems can effectively optimize hydrogel mechanics and modulate the tumor microenvironment.[39,40]

Based on these preliminary studies, we hypothesized that incorporating Ru/SPS and GelMA into the DLM system to construct a DLM–Ru/SPS:GelMA composite bioink would preserve tissue-specific bioactivity while synergistically improving gelation capacity, mechanical properties, and rheological behavior. In this study, we aimed to establish a 3D bioprinted patient-derived CCAO platform for *in vitro* drug-sensitivity screening using this composite bioink. Unlike conventional approaches based on Matrigel embedding or extensive organoid dissociation and reassembly, our strategy employs brief digestion to preserve relatively large patient-derived organoid fragments as the starting material for direct bioprinting, thereby reducing structural disruption and helping maintain multicellular architecture and key phenotypic features. By integrating tissue-specific DLM with mechanically tunable GelMA and employing rapid visible-light-induced crosslinking, this approach is expected to improve printability, structural fidelity, consistency, and reproducibility. Overall, this study aims to overcome a key technical bottleneck in the direct bioprinting of intact patient-derived CCAOs and provide a standardized, reproducible, and biologically relevant platform for drug screening and precision medicine.

2. Materials and methods

2.1. Materials

2.1.1. Human and porcine tissue samples

Cholangiocarcinoma tissues were obtained from patients who underwent surgical resection. In total, three patient-derived CCA organoid lines were established. CCAO-1 was used primarily for platform construction and drug screening, while CCAO-2 and CCAO-3 were used only for final drug testing. The clinicopathological characteristics of the patient-derived CCA samples, including anatomical subtype, tumor differentiation/grade, TNM stage, The American Joint Committee on Cancer pathologic stage, and available information regarding gemcitabine/cisplatin-based treatment response, are summarized in Table S1. The study protocol was approved by the Biomedical Ethics Committee of West China Hospital, Sichuan University, and was conducted in accordance with the Declaration of Helsinki (2023-108).

Normal porcine liver tissues were obtained from a local commercial market in Chengdu, China, as by-products of the food industry and therefore did not require animal ethics approval.

2.1.2 Reagents

Advanced Dulbecco's modified Eagle's medium (DMEM)/F12 (AD), DMEM, fetal bovine serum (FBS), and penicillin-streptomycin (P/S) were purchased from Gibco (United States). Collagenase I, collagenase IV, DNase I, and phalloidin-fluorescein isothiocyanate reagent were obtained from Yeasen Biotechnology Co., Ltd. (China). Matrigel was purchased from Mogengel Bio (China). The Calcein-AM/propidium iodide (PI) Live/Dead staining kit, red blood cell lysis buffer, DAPI staining solution, acridine orange (AO)/PI staining solution, and endotoxin detection kit were purchased from Beyotime Biotechnology (China). MasterAim® Hepatocarcinoma Organoid Complete Medium was obtained from Aimingmed Technology Co., Ltd. (China). The TIANAmp DNA Extraction Kit was purchased from Tiangen Biotech Co., Ltd. (China). The bicinchoninic acid protein assay kit was obtained

from Solarbio Life Sciences (China). The Blyscan Glycosaminoglycan (GAG) Assay Kit and collagen assay kit were purchased from Biocolor Ltd. (United Kingdom). The hematoxylin and eosin (H&E) staining kit and Masson's trichrome staining kit were purchased from Servicebio (China). GelMA (molecular weight: approximately 150 kDa; degree of substitution: 60%) was purchased from Engineering For Life (China).

2.2. Methods

2.2.1. Establishment and culture of patient-derived cholangiocarcinoma organoids

Fresh clinical tissue samples were washed 2–3 times with pre-chilled 1× phosphate-buffered saline (PBS) containing P/S to remove blood, necrotic tissue, and adipose tissue after collection. All initial sample processing was performed under ice-bath conditions. The tissue was minced into approximately 1 mm pieces using sterile blades and digested in a solution containing collagenase I (0.5 mg/mL), collagenase IV (0.5 mg/mL), and DNase I (0.001 mg/mL) at 37 °C with shaking at 80 rpm for 30 min. The digestion was terminated by adding an equal volume of serum-containing AD medium. The digested material was filtered through a 100 μm sterile cell strainer, and the filtrate containing cell clusters was collected. The suspension was centrifuged at 4 °C and 300×g for 5 min; the supernatant was discarded, and the pellet was resuspended in AD medium. If the pellet appeared red, red blood cell lysis buffer was added, and the pellet was incubated on ice for 5 min, then centrifuged again and resuspended. The final suspension was mixed with AO/PI staining solution and analyzed with an automated cell counter to assess cell count and viability. Subsequent culture was performed using MasterAim® Hepatocarcinoma Organoid Complete Medium supplemented with 1% P/S. After viability assessment, the cell clusters were resuspended in complete medium and gently mixed with ice-cold Matrigel at a volume ratio of 3:7. The mixture containing cell clusters equivalent to 1×10^5 cells per well was seeded as 50 μL domes into a pre-warmed 24-well plate using pre-chilled pipette tips. After polymerization at 37 °C for 30 min, each well was overlaid with 500 μL of complete medium. All cultures were maintained at 37 °C in a humidified atmosphere containing 5% carbon dioxide.

2.2.2. Culture of cell lines

L929 mouse fibroblast cells and HepG2 cells were purchased from the American Type Culture Collection (United States). The cells were cultured in DMEM supplemented with 10% FBS and 1% P/S. Cells were maintained at 37 °C in a humidified incubator containing 5% carbon dioxide, and the culture medium was replaced every two days. When the cells reached approximately 80%–90% confluence, they were detached with 0.25% trypsin–ethylenediaminetetraacetic acid and passaged at a 1:3 ratio. Cells in the logarithmic growth phase were used for subsequent experiments.

2.2.3. Preparation of decellularized liver matrix–ruthenium/sodium persulfate:gelatin methacryloyl bioink

Porcine liver tissues were subjected to three freeze-thaw cycles, returned to room temperature, and cut into pieces of approximately 5 × 5 × 5 mm. The tissue pieces were then rinsed three times with sterile water containing 1% P/S for 30 min each until no visible blood remained. Decellularization was performed under magnetic stirring at 200 rpm and 25 °C. Briefly, the tissue pieces were first treated with 1% sodium dodecyl sulfate solution for 24 h, with the solution replaced every 12 h, and then washed with sterile water for six h. The samples were then incubated in 1% Triton X-100 solution for 48–72 h, with solution replacement every 24 h, and subsequently washed again with sterile water for 12 h. Thereafter, the tissues were treated with 60 U/mL DNase I for two h, then washed with sterile water containing P/S for six h to obtain DLM. The obtained DLM was lyophilized for 72 h, ground into powder with a particle size of <1 mm, and stored at −80 °C until use. To prepare the DLM pre-gel, 10 mg of DLM powder was added to 1 mL of 0.1 M hydrochloric acid containing 1 mg/mL pepsin and digested for 72 h at 25 °C and 200 rpm. After digestion, the solution was neutralized to pH 7.4 with 1 N sodium hydroxide and 10× PBS. To prepare the Ru/SPS system, 1.9 mg Ru and 6 mg SPS were dissolved in 10 mL of 1× PBS. The Ru/SPS solution was then mixed with the neutralized DLM pre-gel and stirred until completely homogeneous, yielding the DLM–Ru/SPS bioink, which was stored at 4 °C in the dark. Finally, DLM–Ru/SPS was mixed with GelMA at different ratios to prepare a DLM–Ru/SPS:GelMA bioink, which gelated upon exposure to 405 nm light for 50 seconds using an EFL LS1601 light source operated at 6 V and 2 A. The light source was powered by an SG-060200012A adapter with an output of 6.0 V, 2.0 A, and 12.0 W, where 12.0 W is the device's rated electrical power. The decellularization and enzymatic digestion procedures were adapted from previously reported liver dECM hydrogel protocols.[41-45]

2.2.4. Three-dimensional bioprinting of cholangiocarcinoma organoids

Under ice-bath conditions, DLM and DLM–Ru/SPS:GelMA bioinks were prepared to obtain homogeneous bioink precursors. CCAOs were incorporated into the bioinks

at a density of 2×10^4 organoids/mL and transferred into syringes fitted with 20-gauge nozzles. After equilibration at 4 °C for one h, the bioinks were printed using a BP6602P Bio 3D printer according to the parameters listed in Table 1. The constructs were printed directly into 6-well plates, photocrosslinking under 405nm light for 50 seconds and then cultured in complete medium at 37 °C with 5% carbon dioxide.

Table 1. Three-dimensional bioprinting parameters for decellularized liver matrix–ruthenium/sodium persulfate bioink

Bioink group/ratio (decellularized liver matrix–ruthenium/sodium persulfate:gelatin methacryloyl)	Extrusion pressure (kPa)	Printing speed (mm/min)
Decellularized liver matrix	11	150
1:0	11	150
4:1	11	150
2:1	32	200
3:2	52	200
1:1	76	150
2:3	72	150
1:2	72	150
1:4	83	150

Note. Unless otherwise specified, all groups were printed using bioink maintained at 4 °C in the syringe, a 20 G nozzle, pneumatic extrusion, photocrosslinking at 405 nm for 50 seconds. The bioink ratio indicates the volume ratio of DLM–Ru/SPS to GelMA. DLM represents the DLM-only group without Ru/SPS or GelMA, whereas 1:0 represents the DLM–Ru/SPS group without GelMA.

2.2.5. Scanning electron microscopy

The microstructures of native liver, DLM hydrogel, and DLM–Ru/SPS:GelMA hydrogel were characterized by scanning electron microscopy (SEM; SU5000, Hitachi, Japan). Native liver samples were fixed in 2.5% glutaraldehyde at 4 °C overnight, rinsed three times with PBS, post-fixed with 2% osmium tetroxide for 1–2 h, dehydrated through a graded ethanol series, and dried. DLM and DLM–Ru/SPS:GelMA hydrogel samples were fully immersed in PBS for four h and then lyophilized without chemical fixation, post-fixation, or graded dehydration. All samples were mounted on SEM stubs, sputter-coated with gold, and observed and photographed by SEM to evaluate their microstructural morphology.

2.2.6. Hematoxylin and eosin and Masson's trichrome staining

Paraffin-embedded tissue sections were prepared from porcine liver, porcine DLM, primary human CCA tissues, and patient-derived CCAOs. H&E staining was performed using a commercial H&E staining kit according to the manufacturer's instructions. Briefly, paraffin sections were deparaffinized, rehydrated through a graded ethanol series, stained with hematoxylin and eosin, dehydrated, cleared, and mounted for histological observation.

For Masson's trichrome staining, paraffin sections of porcine liver and porcine DLM were stained using a commercial Masson's trichrome staining kit according to the manufacturer's protocol. After staining, sections were dehydrated, cleared, mounted, and observed under a light microscope.

2.2.7. Immunofluorescence staining

Native liver tissues and decellularized liver tissues were fixed in 4% paraformaldehyde at room temperature (RT) for at least 12 h, embedded in optimal cutting temperature compound, and sectioned into 4-μm-thick cryosections. For organoid samples, organoids embedded in DLM–Ru/SPS:GelMA (4:1) hydrogel were collected together with the surrounding matrix and fixed in 4% paraformaldehyde at RT for 30 min. All samples were then subjected to the same immunofluorescence staining protocol. Except for antibody incubation steps, all procedures were performed at RT. Between each step, samples were gently agitated on a shaker at 60 rpm and washed with PBS three times for 10 min each. Samples were permeabilized with 0.5% Triton X-100 for 30 min, washed again with PBS as described above, and blocked with 5% bovine serum albumin for two h. After blocking, samples were incubated with primary antibodies against Ki67, cytokeratin 7 (CK7), cytokeratin 19 (CK19), zonula occludens-1 (ZO-1), laminin, and fibronectin at a dilution of 1:100 for 24 h at 4 °C. All primary antibodies were rabbit polyclonal antibodies purchased from Proteintech (China). After washing with PBS, samples were incubated with Alexa Fluor 594-conjugated goat anti-rabbit secondary antibodies from Thermo Fisher Scientific (United States), at a dilution of 1:500 for 12 h at 4 °C. Subsequently, F-actin was stained with phalloidin-fluorescein isothiocyanate at a working concentration of 200 nM for one h in the dark at RT, followed by nuclear counterstaining with DAPI at a dilution of 1:100 for 30 min. After staining, tissue sections were mounted with antifade mounting medium, whereas organoid samples were transferred to confocal dishes. Images were acquired using a confocal laser scanning microscope (Ti2, Nikon, Japan). For organoid samples, z-stack imaging was

performed with a step size of 10 μm and a total scan depth of 300 μm.

2.2.8. Photocrosslinking and mechanical properties of decellularized liver matrix–ruthenium/sodium persulfate:gelatin methacryloyl hydrogels

To systematically evaluate the appearance, gelation behavior, photocrosslinking performance, and mechanical properties of DLM–Ru/SPS:GelMA hydrogels with different compositions, composite hydrogel precursor solutions were prepared at DLM–Ru/SPS-to-GelMA volume ratios of 4:1, 2:1, 3:2, 1:1, 2:3, 1:2, and 1:4. The precursor solutions were thoroughly mixed and aliquoted for subsequent characterization. First, to investigate the macroscopic appearance and color variation of hydrogels with different compositions, the precursor solutions were transferred into molds of identical dimensions and photocrosslinked under 405 nm light. After complete gelation, the hydrogels were photographed under identical background and illumination conditions to record their macroscopic morphology, transparency, and color changes. The yellowness index (YI) was calculated from the RGB values of the acquired images using ImageJ software according to the corresponding formula and was used to quantitatively assess the effect of the DLM–Ru/SPS-to-GelMA ratio on the color characteristics of the composite hydrogels. Second, to assess the gelation capability and photocrosslinking performance of the DLM–Ru/SPS:GelMA systems, the precursor solutions were loaded into centrifuge tubes for gelation testing. The samples were subjected to two different curing conditions: one group was incubated at 37 °C under ambient light for 30 min, whereas the other group was exposed to 405 nm light at room temperature for 50 seconds. After curing, the tubes were inverted to determine whether the samples remained flowable, thereby evaluating the gel formation ability and structural stability of hydrogels with different compositions. Representative images were recorded to compare the gelation behavior under different curing conditions. Finally, to further characterize the mechanical properties of the DLM–Ru/SPS:GelMA hydrogels, the Young's modulus was used as an indicator of material stiffness. The precursor solutions were cast into cylindrical molds with a height of 3 mm and a diameter of 7 mm, then photocrosslinked under 405 nm light. After complete gelation, uniaxial compression tests were performed using a mechanical tester (EFL-MT5600, China) at RT. The samples were compressed at a speed of 1 mm/min until the maximum load reached 1 N. Young's modulus was determined from the slope of the initial linear region of the stress–strain curve.

The rheological properties of the bioinks were measured using a modular compact rheometer MCR302 (Anton Paar, Austria) equipped with a 25-mm parallel-plate geometry. Bioink samples were carefully loaded onto the lower plate, and the measuring gap was adjusted to ensure complete contact between the sample and the upper plate. Excess material was gently removed from the edge of the plate before testing. Dynamic oscillatory frequency-sweep tests were performed to evaluate the viscoelastic properties of various bioink formulations. The strain amplitude was set at 1%, which was within the linear viscoelastic region. The frequency was swept from 0.01 to 1 Hz, and the storage modulus (G′), loss modulus (G″), and complex viscosity (η*) were recorded as functions of frequency. The frequency-dependent changes in G′, G″, and η* were used to compare the viscoelastic behavior and printability-related rheological properties of different DLM–Ru/SPS:GelMA formulations. All rheological measurements were performed in triplicate.

2.2.9. Cell viability and morphology assessment in three-dimensional constructs

L929 cells and CCAOs encapsulated in 3D gel droplets or 3D-printed constructs were subjected to Live/Dead staining to evaluate cell viability. Bright-field imaging using an inverted optical microscope was performed to monitor organoid morphology and changes in organoid number. For 3D gel droplet culture, L929 cells or CCAOs were gently mixed with ice-cold DLM–Ru/SPS bioink. The final concentration of L929 cells in the bioink was 200,000 cells/mL, while CCAOs were suspended at 20,000 organoids/mL. Subsequently, 30 μL of the cell- or organoid-laden bioink was deposited into each well of a 48-well plate to form 3D gel droplets. After gelation, 250 μL of the corresponding culture medium was added to each well, and the samples were maintained in a humidified incubator at 37 °C with 5% carbon dioxide. The 3D-printed constructs were prepared as described above, transferred to culture plates, supplied with the corresponding culture medium, and maintained under standard culture conditions.

Bright-field images were acquired at the indicated time points using an inverted optical microscope (Zeiss, Germany) to observe organoid morphology and quantify changes in organoid number under different culture conditions. Meanwhile, cell viability was assessed using a calcein-AM/PI Live/Dead staining assay. Briefly, the working staining solution was prepared by adding 3 μL calcein-AM and 2 μL propidium iodide to 1 mL PBS. After removal of the culture medium, each sample was incubated with 500 μL of staining solution for 30 min at 37 °C in the dark. After staining, the samples were gently washed with PBS and subjected to fluorescence imaging. L929 cells and CCAOs were imaged using both a BioTek

Cytation C10 confocal imaging reader (BioTek, United States) and a confocal laser scanning microscope (Ti2, Nikon, Japan). For organoid samples, Z-stack imaging was performed with a step size of 10 μm and a total scan depth of 300 μm. Live cells were stained green, whereas dead cells were stained red.

2.2.10. Drug screening

After three days of culture, the medium in the 3D constructs was replaced with fresh medium containing different drug concentrations to evaluate cytotoxic effects on CCAOs. The experimental groups included cisplatin monotherapy and cisplatin plus gemcitabine. For the combination treatment group, cisplatin and gemcitabine were simultaneously added to the culture medium, with each drug used at final concentrations of 1, 10, and 100 μM. For the combination treatment group, cisplatin and gemcitabine were simultaneously added to the culture medium at final concentrations of 1, 10, and 100 μM, respectively. After 72 h of drug treatment, Live/Dead staining was performed, and cell viability as well as drug-induced morphological changes were observed.

2.2.11. Statistical analysis

All data are presented as the mean ± standard deviation. Unless otherwise stated, n represents the number of independent biological replicates. Statistical analysis was performed using GraphPad Prism 10.4.3 (United States). Unpaired comparisons were conducted using the t-test, and multiple-group comparisons were performed using one-way analysis of variance followed by Tukey's post-hoc test. Statistical significance was defined as $^{*}p < 0.05$, $^{**}p < 0.01$, $^{***}p < 0.001$, and $^{****}p < 0.0001$.

3. Results and discussion

3.1. Characterization of decellularized liver matrix

Cholangiocarcinoma is characterized by high invasiveness, pronounced interpatient heterogeneity, and poor clinical prognosis, resulting in substantial variability in therapeutic responses. Therefore, there is an urgent need for in *vitro* drug-screening platforms that more faithfully recapitulate patient-specific tumor features. Notably, the initiation, progression, and therapeutic responsiveness of CCA are strongly regulated by the tumor microenvironment rather than by tumor cells alone. Accordingly, the development of a more predictive patient-derived organoid bioprinting platform requires faithful reconstruction of the native microenvironment associated with CCA, particularly tissue-specific ECM cues. Based on this rationale, we first prepared DLM from native liver tissue (Figure 1) and systematically characterized its decellularization efficiency, ECM retention, and structural stability to determine whether it could serve as the core biological component of the subsequent printable composite bioink.

As shown in Figure 2A, the prepared DLM exhibited a homogeneous, translucent, gel-like appearance. Quantification of DNA and protein contents showed a significant reduction in DLM compared with native liver tissue (Figure 2B). H&E staining revealed clearly visible nuclei in native liver tissue, whereas nuclear signals were markedly diminished in DLM (Figure 2C), confirming successful decellularization. SEM revealed an open porous network within the DLM (Figure 2C), indicating a structural architecture favorable for cell loading and mass transfer. Importantly, Masson's trichrome staining still revealed the presence of collagen fibers in the DLM (Figure 2D). Further immunofluorescence analysis demonstrated the retention of major ECM components, including fibronectin and laminin (Figure 2D), suggesting that the DLM preserved key features of the liver-derived matrix. In addition, quantitative analysis showed that total protein, collagen, and GAG were retained to a considerable extent in the DLM (Figures 2B and 2E). As an essential functional component of the ECM, GAG remained at a biologically meaningful level, indicating that the DLM preserved not only structural support elements but also bioactive cues relevant to cell adhesion, migration, and microenvironmental regulation.

Given that this material would subsequently be used for composite bioink fabrication and organoid bioprinting, we further evaluated its biosafety, batch consistency, and structural stability. The residual endotoxin levels in DLM were low (0.5 EU/mL) and showed no significant batch-to-batch differences (Figure 2F). Although the porcine livers used in this study were obtained from a local commercial food market, which may introduce uncontrolled biological variables such as animal age, strain, and warm post-mortem ischemia time, batch-to-batch reproducibility of the DLM-based bioink was managed through standardized processing and quality-control assessment. Specifically, all liver tissues were processed using the same decellularization, washing, lyophilization, milling, digestion, and neutralization procedures. For each DLM batch, key quality-control parameters, including gross appearance after decellularization, residual DNA content, ECM component retention, gelation behavior, rheological properties, and endotoxin levels, were evaluated before experimental use. Only batches that met these quality-control criteria were used for subsequent organoid culture and bioprinting experiments. These procedures helped minimize batch-dependent variability and ensured the reproducibility of the DLM bioink for downstream

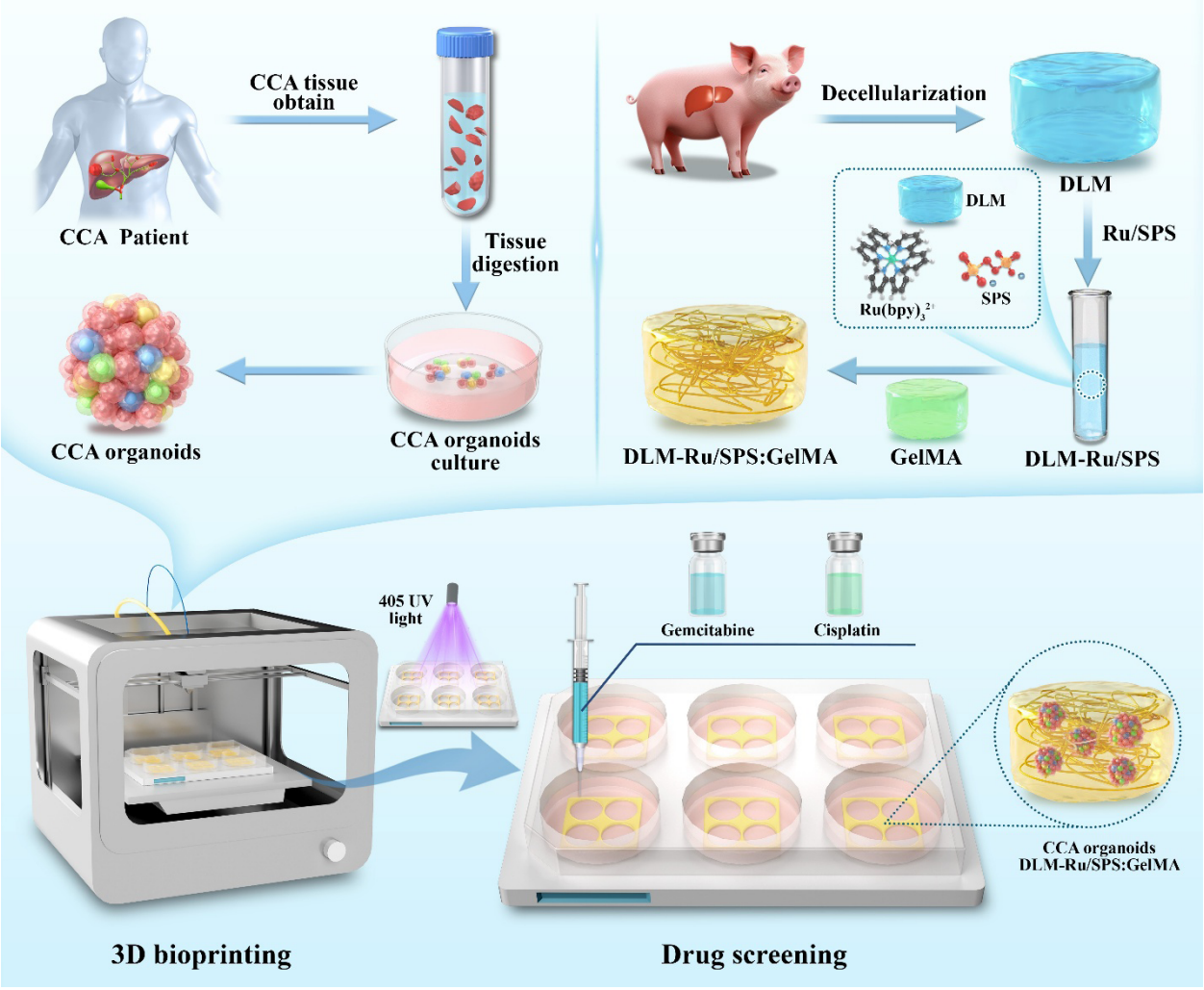

Figure 1. Schematic illustration of the preparation of DLM–Ru/SPS:GelMA bioink and its application in 3D bioprinting-based drug screening. Porcine liver tissue was decellularized to obtain DLM, which was subsequently combined with Ru/SPS and GelMA to formulate a photocrosslinkable DLM–Ru/SPS:GelMA bioink. Patient-derived CCA tissues were enzymatically digested, isolated, and cultured to obtain patient-derived CCAOs, which were then incorporated into the bioink. The CCAO-laden bioink was deposited into 6-well plates using a 3D bioprinter and photocrosslinked under 405 nm light to generate bioprinted CCAO constructs. The resulting organoid constructs were further applied for *in vitro* drug screening.
Abbreviations: 3D: Three-dimensional; CCA: Cholangiocarcinoma; CCAO: Cholangiocarcinoma organoid; DLM: Decellularized liver matrix; GelMA: Gelatin methacryloyl; Ru: Ruthenium; SPS: Sodium persulfate.

applications.

To further evaluate the biocompatibility of DLM, HepG2 cells were cultured in DLM hydrogels and cell viability was assessed on days 1, 3, and 7 (Figure S1). The results showed that HepG2 cells maintained high viability (>90%) throughout the culture period, with no significant differences among time points, indicating the favorable biocompatibility of DLM. In addition to HepG2 cells, normal mouse liver organoids were cultured in DLM hydrogels to further assess the ability of DLM to support 3D organoid growth. Matrigel, a widely used ECM for organoid culture, served as a control. As shown in Figure S2, mouse liver organoids embedded in DLM exhibited robust growth and progressive expansion over the culture period, with a morphology comparable to that of organoids cultured in Matrigel. Quantitative analysis showed that DLM supported organoid formation and growth, although early organoid numbers were lower than those in the Matrigel group at some time points, indicating an initial delay in organoid expansion within the DLM hydrogel.

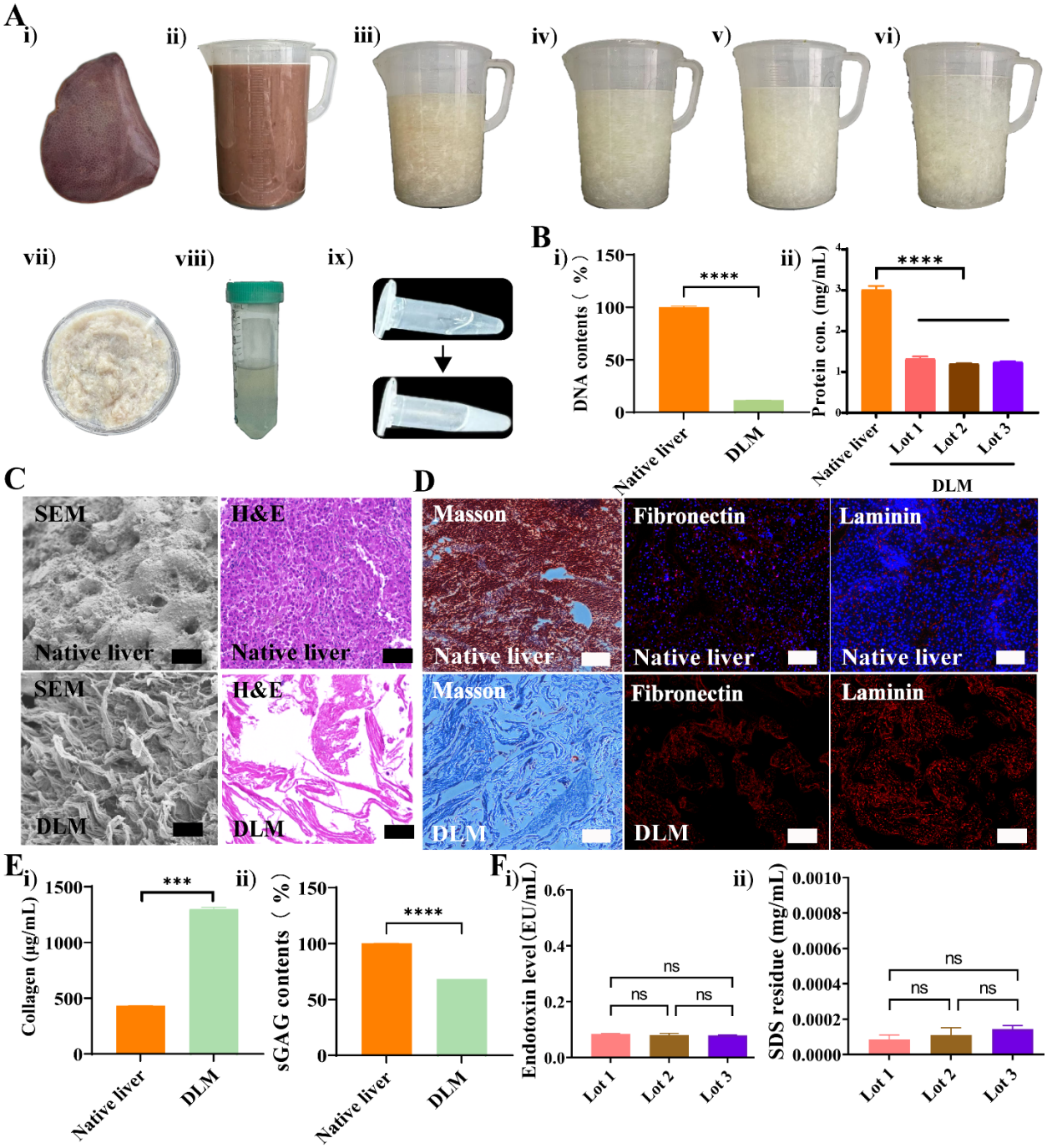

Figure 2. Structural and compositional characterization of liver-derived scaffolds before and after decellularization. (A) Schematic illustration of the DLM preparation process (i–ix), including (i) liver, (ii) liver tissue fragmentation, (iii) PBS perfusion, (iv) SDS treatment, (v) Triton X-100 perfusion, (vi) DNase treatment, (vii) lyophilization, and (viii–ix) gelation. Step (viii) indicates enzymatic digestion, and black arrows in step (ix) indicate the transition of DLM into a gel. (B) Quantitative analysis of (i) DNA and (ii) protein contents before and after decellularization. (C, D) Representative SEM images, H&E staining, Masson's trichrome staining, and immunofluorescence staining of fibronectin (red) and laminin (red) before and after decellularization. Nuclei were counterstained with DAPI (blue). Scale bar: 200 μm; magnification: 4×. (E) Quantitative analysis of (i) collagen and (ii) sGAG contents before and after decellularization. (F) Endotoxin levels (i) and SDS residue (ii) in three lots of DLM. Quantitative data are presented as mean ± standard deviation from $n = 3$ independent biological replicates unless otherwise indicated. Statistical significance is indicated as follows: ns, not significant; $^{***}p < 0.001$, $^{****}p < 0.0001$.

Abbreviations: DLM: Decellularized liver matrix; H&E: Hematoxylin and eosin; PBS: Phosphate-buffered saline; SDS: Sodium dodecyl sulfate; SEM: Scanning electron microscopy; sGAG: Sulfated glycosaminoglycan.

Nevertheless, organoid diameter increased over time in the DLM group, supporting its ability to maintain organoid growth after the initial adaptation phase. These results suggest that DLM provides a suitable microenvironment for maintaining the viability and growth of normal mouse liver organoids, further confirming its good biocompatibility and potential as an alternative matrix for liver organoid culture. Collectively, these results indicate that DLM effectively removes cellular components while preserving key liver ECM constituents, including GAG, and exhibits favorable biosafety, thereby providing a robust foundation for the construction of a tissue-specific 3D bioprinting platform.

3.2. Characterization of the decellularized liver matrix–ruthenium/sodium persulfate:gelatin methacryloyl composite bioink

After confirming that DLM preserves liver-specific ECM components and exhibits favorable bioactive properties, we next focused on a critical limitation of its use as a bioink: insufficient mechanical support and rapid shape fixation, which still fall short of the requirements for extrusion-based bioprinting in terms of printability and structural stability. This issue is particularly pronounced for the direct bioprinting of patient-derived CCAOs, as the material must not only retain biological cues but also maintain a stable 3D architecture after deposition. To address this challenge, we incorporated a Ru/SPS visible-light crosslinking system into the DLM-based formulation. In our previous work, we demonstrated that the introduction of Ru/SPS enabled rapid gelation of decellularized kidney matrix within 40 seconds under 405 nm illumination, together with favorable biocompatibility. Based on this validated system, we hypothesized that the same strategy could be applied to DLM to improve its gelation kinetics and printability while preserving its tissue-specific biological advantages.

First, we evaluated the temporal stability of DLM–Ru/SPS in solution. The results showed that the system maintained a similar appearance on day 1, day 3, day 5, and day 20, with no significant differences in diameter or area among the different time points (Figure S3), indicating good solution stability and providing an operational window for subsequent loading of CCAOs and 3D printing. In addition, GelMA was introduced as an additional network-forming component to enhance the tunability and printability of the composite system. To identify the optimal bioink formulation for 3D printing and growth of CCAOs, we systematically characterized the properties of bioinks with different component ratios.

First, we examined the appearance of the composite bioinks at different ratios. The results showed that, as the GelMA content increased, the appearance of the composite bioink changed progressively, reflecting a clear composition-dependent behavior in the DLM–Ru/SPS:GelMA system. Quantitative analysis of the YI further confirmed significant optical differences among the formulations (Figure 3A), indicating that stable and reproducible bioinks could be obtained by adjusting the DLM-to-GelMA ratio. Although this optical variation itself is not a direct functional endpoint, it suggests that the hydrogel network can be reliably modulated, which is beneficial for establishing a standardized printing platform.

Meanwhile, unmodified DLM, DLM–Ru/SPS, and DLM–Ru/SPS:GelMA samples with different ratios all exhibited typical nonlinear stress–strain behavior in tensile testing, but their load-bearing capacity and pre-fracture mechanical responses differed substantially (Figure S4). The Young's modulus results showed that the stress-response capacity of the composite hydrogels increased significantly with changes in GelMA content (Figure 3B), indicating that the incorporation of GelMA effectively modulates network density and overall mechanical performance. In particular, at higher GelMA ratios, the system exhibited stronger load-bearing capacity and a more pronounced network reinforcement effect, suggesting that the mechanical window of this composite bioink can be tuned from softer to stiffer states through formulation optimization. This tunable mechanical behavior is especially important for 3D tumor organoid platforms: appropriate stiffness helps maintain printed structures and prevents collapse during culture, whereas excessive stiffness may restrict organoid expansion or alter tumor cell behavior. Therefore, the mechanical tunability of the DLM–Ru/SPS:GelMA system provides a basis for constructing an organoid bioprinting platform with both structural stability and biocompatibility.

To further clarify the viscoelastic behavior and the printability mechanism of the composite bioink, frequency-sweep rheological measurements were performed on DLM–Ru/SPS:GelMA formulations at different volumetric ratios. As shown in Figure S5, the storage modulus G′, loss modulus G″, and complex viscosity η* exhibited clear frequency-dependent and composition-dependent variations, indicating that the rheological properties of the bioink could be effectively regulated by adjusting the formulation. Among these groups, the 4:1 formulation maintained a favorable balance between elasticity and flowability, which is particularly important for extrusion-based bioprinting because it supports smooth extrusion while preserving filament fidelity after deposition. These rheological results further support the printability of the composite bioink and are consistent with the subsequent

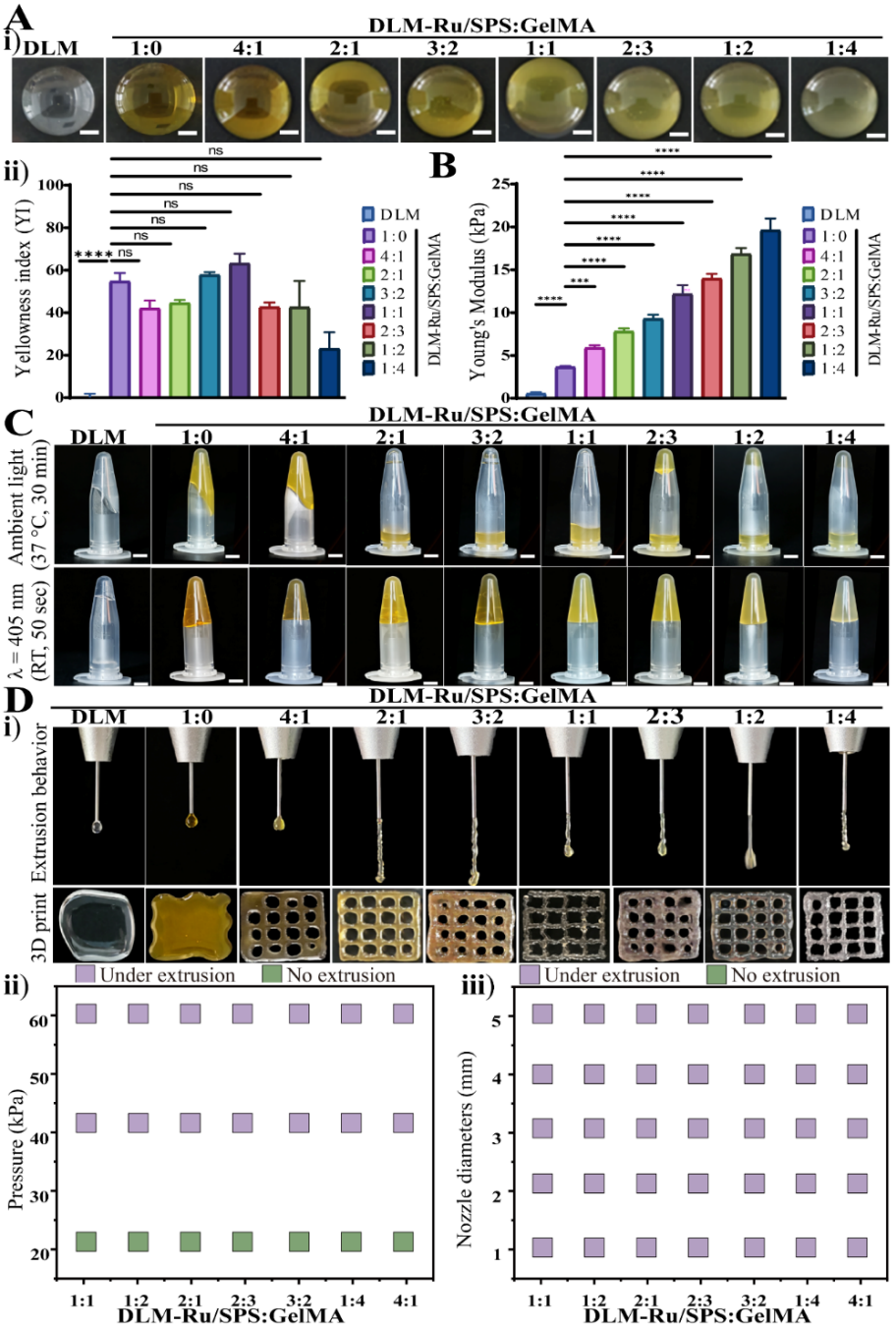

Figure 3. Characterization of DLM–Ru/SPS:GelMA composite bioinks. (A) Representative photographs of DLM and DLM–Ru/SPS:GelMA bioinks with different mixing ratios. (i) Macroscopic appearance of the bioinks. (ii) Quantitative analysis of the yellowness index. Scale bars: 2.5 mm. (B) Young's modulus of DLM and DLM–Ru/SPS:GelMA bioinks with different ratios. (C) Representative images showing the gelation behavior of DLM and DLM–Ru/SPS:GelMA formulations under ambient light at 37 °C for 30 min and under 405 nm light irradiation for 50 seconds. Scale bars: 5 mm. (D) Printability assessment of the composite bioinks. (i) Representative extrusion behavior and printed grid structures of DLM and DLM–Ru/SPS:GelMA bioinks. (i) Representative extrusion behavior and printed grid structures of DLM and DLM–Ru/SPS:GelMA bioinks with different ratios. (ii, iii) Printability maps showing the extrusion conditions as a function of pressure and nozzle diameter, with purple and green indicating under-extrusion and no extrusion, respectively. Quantitative data are presented as mean ± standard deviation from $n = 3$ independent biological replicates unless otherwise indicated. Statistical significance is indicated as follows: ns, not significant; ***$p < 0.001$, ****$p < 0.0001$.
Abbreviations: DLM: Decellularized liver matrix; GelMA: Gelatin methacryloyl; Ru: Ruthenium; SPS: Sodium persulfate.

printing performance.

Next, we assessed the gelation capability of the composite bioinks with different compositions. The results showed that DLM alone and DLM–Ru/SPS, when used independently, exhibited only limited gelation even after incubation at 37 °C for 30 min. The addition of GelMA did not further enhance this thermally induced gelation behavior. In contrast, upon introduction of the Ru/SPS photoinitiation system, both DLM–Ru/SPS and the DLM–Ru/SPS:GelMA mixtures underwent rapid gelation within 50 seconds under 405 nm light irradiation. These findings demonstrate that the Ru/SPS visible-light crosslinking system is essential for achieving rapid and controllable solidification (Figure 3C). Further temperature-responsiveness testing showed that, at 37 °C, DLM–Ru/SPS:GelMA formulations with different ratios exhibited distinct degrees of state transition over 0, 10, 20, and 30 min (Figure S6), suggesting that the fluidity and preliminary solidification behavior of this bioink are jointly regulated by temperature and component ratio, thereby maintaining appropriate flowability prior to printing. Notably, thermoresponsive behavior alone is insufficient to ensure final structural fixation. Overall, the DLM–Ru/SPS:GelMA system combines solution stability, thermoresponsiveness, and rapid light-triggered gelation, thereby providing a foundation for developing a printable and standardized organoid biomanufacturing platform.

To further verify the behavior of this system under practical printing conditions, we next evaluated its extrusion-based printability using a 3D printer. The results showed that neither DLM nor DLM–Ru/SPS was printable. After introducing GelMA, all DLM–Ru/SPS:GelMA formulations became printable to varying degrees; however, as the GelMA ratio increased, filament continuity decreased, and the printed structures became less well-defined. This behavior may be related to the specific low-temperature extrusion conditions used here, under which increased GelMA content could alter local gelation behavior, optical transparency, and filament continuity. The printability map corresponding to pressure and nozzle parameters further indicated that the printable region was significantly influenced by the bioink composition (Figure 3D). These results suggest that stable organoid bioprinting requires not only optimization of the material formulation but also coordination with printing parameters, which is critical for translational applications.

The primary application of this study is 3D bioprinting of CCA. In summary, the DLM–Ru/SPS:GelMA bioink achieves a balance among solution stability, thermoresponsiveness, gelation kinetics, mechanical tunability, and print fidelity through rational optimization, supporting its feasibility as a bioprinting material. More importantly, this optimization strategy overcomes the intrinsic limitation of insufficient gelation in DLM, enabling its application in engineered biomanufacturing.

3.3. Optimization of decellularized liver matrix–ruthenium/sodium persulfate:gelatin methacryloyl bioink for cholangiocarcinoma organoid culture

In our previous work, we successfully developed a DLM–Ru/SPS:GelMA composite bioink with favorable performance and demonstrated that tuning the DLM–Ru/SPS-to-GelMA ratio effectively modulated its mechanical properties and printability. Building on this foundation, the present study further evaluated the biological applicability of the bioink, namely whether it could provide a suitable three-dimensional microenvironment for CCAOs while maintaining organoid viability and facilitating subsequent observation and analysis. Given that the organoids, the selection of the material should not rely solely on print fidelity or mechanical strength, but rather require a comprehensive evaluation of printing stability, biocompatibility, organoid growth behavior, and microscopic imaging readability.

First, L929 cells were used for preliminary biocompatibility screening of DLM–Ru/SPS:GelMA hydrogels with different formulations. The results showed that L929 cells maintained high viability in all hydrogel groups, with no obvious cell death observed, indicating that this composite system exhibits good baseline biocompatibility and may serve as a safe material platform for subsequent organoid culture (Figure 4A).

Next, hydrogels with different formulations were further applied to CCAO culture to assess their practical suitability in the target model. The results showed that all hydrogel groups supported the formation and maintenance of CCAOs, demonstrating the basic feasibility of the DLM–Ru/SPS:GelMA composite system as a 3D matrix for organoid culture. To further benchmark its performance against a conventional matrix, Matrigel-cultured CCAOs were included as a control. Comparative analysis revealed that the DLM–Ru/SPS:GelMA 4:1 group exhibited larger organoid diameters and a higher number of organoids than the Matrigel group at the evaluated time points, while maintaining a comparable level of cell viability, as confirmed by Live/Dead staining and quantitative viability analysis (Figure 4B and 4C). These findings indicate that the 4:1 bioink not only supports organoid survival at a level comparable to Matrigel, but also more effectively promotes organoid growth and expansion.

However, distinct differences were observed among the formulations in organoid culture and visualization.

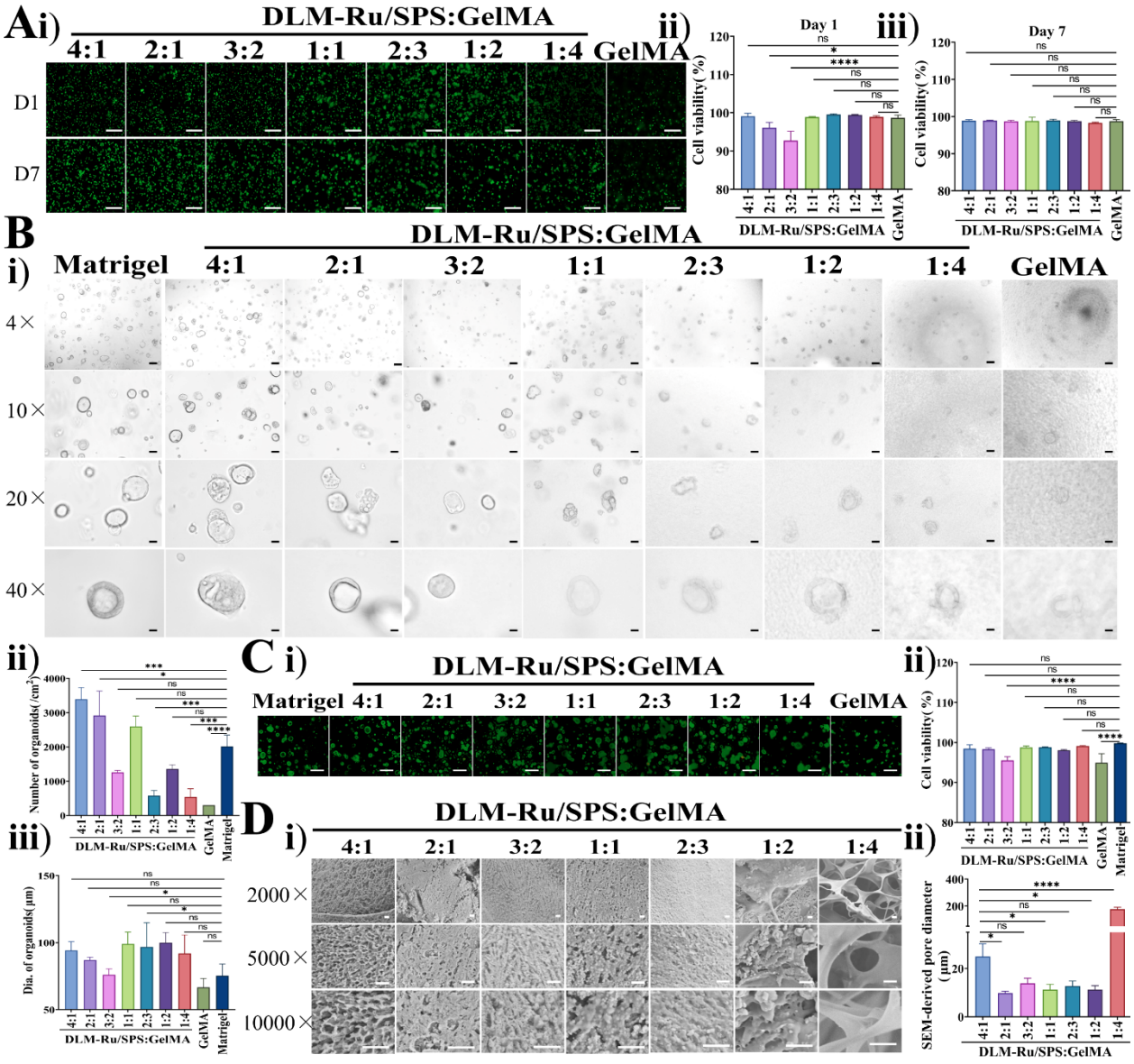

Figure 4. Biocompatibility evaluation of DLM–Ru/SPS:GelMA hydrogels. The hydrogel was photopolymerized under 405-nm light irradiation for 50 seconds. (A) Calcein-AM/PI Live/Dead staining of L929 cells cultured in different hydrogel droplet culture systems, including GelMA and DLM–Ru/SPS:GelMA hydrogels, after 1 and 7 days. Representative image (i) and quantitative analysis (ii, iii) are shown. Live cells are shown in green and dead cells in red. Scale bar: 500 μm; magnification: 4×. (B) Morphological analysis of CCAOs cultured in different hydrogel droplet culture systems, including Matrigel, GelMA and DLM–Ru/SPS:GelMA hydrogels, after 1 day. (i) Representative bright-field images are shown at magnifications of 4×, 10×, 20×, and 40×. Scale bar: 100 μm for 4× magnification; 40 μm for 10× magnification; 20 μm for 20× magnification; and 10 μm for 40× magnification. Quantitative analysis of the number (ii) and diameter (iii) of CCAOs. (C) Calcein-AM/PI Live/Dead staining of CCAOs cultured in different hydrogel droplet culture systems, including Matrigel, GelMA and DLM–Ru/SPS:GelMA hydrogels, after 1 day. Representative image (i) and quantitative analysis (ii) are shown. Scale bar: 500 μm; magnification: 4×. (D) SEM analysis of DLM–Ru/SPS:GelMA hydrogels. (i) Representative SEM images are shown at magnifications of 2,000×, 5,000×, and 10,000×. Scale bar: 20 μm for all magnifications. (ii) Quantitative analysis of the pore diameter. Quantitative data are presented as mean ± standard deviation from $n = 3$ independent biological replicates unless otherwise indicated. Statistical significance is indicated as follows: ns, not significant; $^{*}p < 0.05$, $^{***}p < 0.001$, $^{****}p < 0.0001$.

Abbreviations: CCAO: Cholangiocarcinoma organoid; DLM: Decellularized liver matrix; GelMA: Gelatin methacryloyl; PI: Propidium iodide; Ru: Ruthenium; SEM: Scanning electron microscopy; SPS: Sodium persulfate.

With increasing GelMA content, the transparency of the hydrogel network gradually decreased, resulting in reduced visibility of organoids under bright-field microscopy, as evidenced by increased background intensity, blurred boundaries, and difficulty in contour recognition. Quantitative analysis of organoid number and diameter further revealed formulation-dependent differences in organoid formation efficiency and growth behavior, suggesting that material composition influences the 3D microenvironment surrounding the organoids (Figure 4B). To further clarify the structural basis underlying the observed differences in organoid visualization and growth among formulations, the internal microarchitecture of the DLM–Ru/SPS:GelMA hydrogels was examined by scanning electron microscopy. As shown in Figure 4D, the samples with different ratios exhibited pronounced composition-dependent differences in pore structure and network connectivity. The high DLM–Ru/SPS-content group exhibited a relatively dense, compact network with smaller pores, whereas increasing the GelMA content led to a progressively looser internal structure, larger pore sizes, and enhanced network connectivity. In the group with the highest GelMA content, a more open porous structure with thinner pore walls was observed, indicating a substantially more porous microarchitecture. These findings demonstrate that the pore structure and network density of the composite hydrogels can be effectively regulated by adjusting the DLM–Ru/SPS-to-GelMA ratio.

Taken together, the reduction in transparency observed with increasing GelMA content may be attributed to the denser microstructure, altered network organization, and the resulting enhancement of light scattering within the hydrogel. In contrast, the 4:1 formulation exhibited a relatively homogeneous, moderate microstructure, providing sufficient 3D support while enabling better light transmission and organoid visualization, thereby offering superior performance in both organoid culture and imaging readability. Moreover, these microstructural differences may not only affect optical transparency, but also influence the diffusion of nutrients, oxygen, and metabolic waste, thereby impacting organoid formation, maintenance, and expansion. Compared with Matrigel, the 4:1 formulation achieved a better balance between structural support and spatial openness, making it more suitable as a matrix for 3D culture and subsequent drug screening of CCAOs. Collectively, based on the material characterization results, biocompatibility evaluation, and organoid culture performance, the 4:1 formulation was identified as the optimal DLM–Ru/SPS:GelMA bioink ratio in this study.

3.4. Bioprinting-enabled generation of viable spheroidal cholangiocarcinoma organoids

Building on the aforementioned material characterization, biocompatibility evaluation, and organoid culture results obtained across different formulations, the 4:1 DLM–Ru/SPS:GelMA ratio was identified as the optimal composition for structural support, shape fidelity, and biological compatibility. Accordingly, this formulation was selected for subsequent evaluations of the DLM–Ru/SPS:GelMA bioink in the 3D bioprinting of CCAOs. Unlike conventional biomaterials designed primarily to maximize mechanical strength, organoid bioprinting requires a bioink that can simultaneously support cell self-organization, proliferation, and tissue-like remodeling. Therefore, a formulation that balances printability and biological functionality is particularly valuable for organoid engineering.

To further assess the impact of the printing environment on organoid viability, Live/Dead staining was performed. Most cells exhibited AM-positive green fluorescence, with only a small fraction of PI-positive cells, indicating low levels of cell death in the printed organoids (Figure 5 and 5B). Quantitative analysis revealed that organoid viability in the 4:1 group remained high during culture (Figure S7A and S7B). This result is significant because it suggests that the optimized formulation provides sufficient mechanical support without imposing substantial cytotoxic stress on the cells. In addition, the hydrogel microenvironment appears to permit adequate nutrient diffusion and waste removal, both of which are essential for sustaining organoid growth in a 3D setting. For bioprinting applications, achieving this balance between structural stability and cellular permissiveness is critical: overly dense networks may preserve the printed shape but hinder proliferation and remodeling, whereas overly loose matrices may fail to maintain structural integrity. The formulation appears to strike an appropriate balance between these two requirements.

Representative images (Figure 5C) at different magnifications illustrate the progressive maturation of the organoid morphology, while quantitative analysis showed that both the number and diameter of the printed organoids remained within a relatively stable range, indicating good reproducibility and structural consistency (Figure S7C). Organoids printed with the formulation gradually developed into compact spheroidal structures with well-defined boundaries during culture. Importantly, the 3D reconstruction presented in Figure 5D further confirmed this morphology from a spatial perspective.

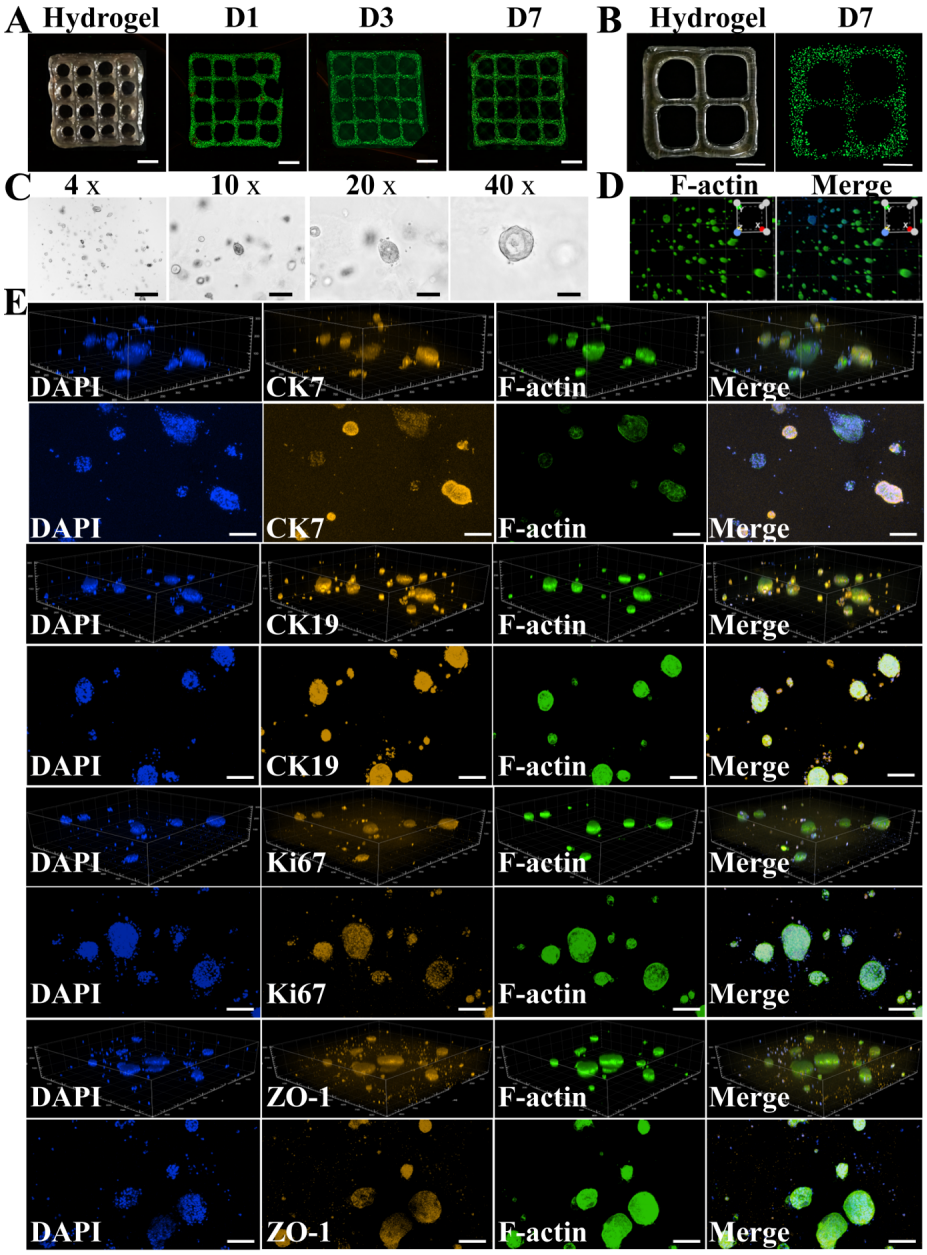

Figure 5. Viability and phenotypic preservation of 3D-bioprinted CCAOs in DLM–Ru/SPS:GelMA (4:1) hydrogels. The CCAO-laden hydrogel was photocrosslinked under 405-nm light irradiation for 50 seconds. (A) Bright-field and calcein-AM/PI Live/Dead staining images of 3D bioprinted CCAO-laden hydrogels with a 4 × 4 grid structure on day 1, 3 and 7. Scale bar: 5 mm. (B) Bright-field and calcein-AM/PI Live/Dead staining images of 3D bioprinted CCAO-laden hydrogels with a 2 × 2 grid structure on day 7. Scale bar: 5 mm. In calcein-AM/PI staining images, live cells are shown in green and dead cells in red. (C) Bright-field images of CCAOs at 4×, 10×, 20×, and 40× magnifications. Scale bar: 100 μm for the 4× image. (D) Representative confocal z-stack-derived 3D-rendered images of CCAOs stained with DAPI for nuclei and phalloidin-FITC for F-actin/cytoskeleton visualization, along with merged fluorescence images. The reconstructed viewing volume was 500 μm × 500 μm × 300 μm. (E) Representative confocal z-stack-derived 3D reconstructions and 2D fluorescence projection images of CCAOs stained for DAPI, CK7, CK19, Ki67, ZO-1, and F-actin. F-actin/cytoskeleton was visualized using phalloidin-FITC staining. Nuclei are shown in blue; F-actin/cytoskeleton is shown in green by phalloidin-FITC staining; and CK7, CK19, Ki67, and ZO-1 are shown in orange-yellow. The reconstructed viewing volume was 900 μm × 900 μm × 300 μm. Scale bars: 100 μm for the 2D images.
Abbreviations: 2D: Two-dimensional; 3D: Three-dimensional; CCAO: Cholangiocarcinoma organoid; CK7: Cytokeratin 7; CK19: Cytokeratin 19; DLM: Decellularized liver matrix; F-actin: Filamentous actin; FITC: Fluorescein isothiocyanate; GelMA: Gelatin methacryloyl; PI: Propidium iodide; Ru: Ruthenium; SPS: Sodium persulfate; ZO-1: Zonula occludens-1.

The uniformly distributed DAPI and phalloidin signals outlined a multicellular architecture with clear thickness and spatial hierarchy, demonstrating that the printed structures were not merely circular in 2D projection, but true spheroidal organoids formed within the hydrogel matrix. This is particularly relevant for CCA modeling, as such a spheroidal architecture more closely resembles *in vivo* tumor organization and may better recapitulate cell–cell interactions, diffusion gradients, and signaling behaviors that are critical for downstream functional studies.

Furthermore, H&E staining was performed to further evaluate whether the printed organoids retained the histological characteristics of the matched primary patient tumor tissue. The results showed that the 3D printed tumor organoids exhibited histopathological features consistent with those of the original tumor tissue (Figure S9). In particular, the printed organoids recapitulated several characteristic histological features of CCA tissue, including atypical epithelial tumor-cell morphology, glandular/lumen-like structures, and organized tissue-like architecture resembling the matched primary tumor. These findings provide direct histological evidence that the 3D-printed organoids retained key morphological characteristics of the patient-derived tumor following printing and culture.

We next examined whether the printed organoids retained key CCA-associated phenotypic features. As shown in Figure 5E and Figure S8, CK7 and CK19 staining supported the maintenance of biliary epithelial features in the printed organoids. In addition, Ki67 positivity indicated sustained proliferative activity, suggesting that the organoids remained biologically active in the 3D hydrogel environment. Notably, ZO-1 staining suggested partial maintenance or re-establishment of epithelial organization after printing.

Taken together, these findings indicate that the DLM–Ru/SPS:GelMA bioink does more than serve as a passive structural support; rather, it provides a functional microenvironment that supports not only cell survival but also the preservation of tissue-level organization and tumor-associated phenotype. This is an important feature for organoid-based tumor models, as maintaining epithelial architecture and polarity-related components, such as ZO-1, may enhance physiological relevance.

In summary, the optimized DLM–Ru/SPS:GelMA bioink supported the formation of stable spheroidal CCAOs while maintaining high cell viability, representative phenotypic markers, and structural integrity after printing. These results underscore the advantage of this formulation in achieving a favorable balance between mechanical performance, cytocompatibility, and tissue-mimetic capacity, thereby supporting its potential utility as a robust platform for three-dimensional CCAO bioprinting and subsequent applications such as drug testing and personalized disease modeling.

3.5. Drug sensitivity evaluation of bioprinted cholangiocarcinoma organoids

In the preceding experiments, we demonstrated that the optimized DLM–Ru/SPS:GelMA bioink supported the formation of stable spherical 3D CCAOs that maintained high cell viability and retained expression of cholangiocyte-related phenotypic markers during short-term culture. These findings indicate that the bioprinting system not only enables spatial reconstruction of the 3D organoid architecture, but also preserves the biological characteristics of the tumor cells at the functional level. On this basis, we further considered whether this model could serve not only as a platform for organoid construction and culture but also as a translationally relevant drug-evaluation system to simulate CCA responses to commonly used clinical chemotherapeutic agents. Since drug sensitivity is a critical parameter for determining whether organoid models can truly support precision medicine, pharmacological validation of this model after structural and phenotypic characterization is of substantial importance.

Among the first-line chemotherapeutic regimens for CCA, cisplatin and gemcitabine are among the most widely used drug combinations. Therefore, cisplatin was first applied as a single-agent intervention to the printed organoids to assess the model's morphological and viability responses to chemotherapeutic stimulation. Subsequently, the effects of combined cisplatin and gemcitabine treatment were examined to determine whether this 3D bioprinted system could capture dose- and combination-dependent responses to commonly used chemotherapeutic agents. In other words, this set of experiments was designed not merely to determine whether the drugs were "effective," but, more importantly, to evaluate whether the printed organoids could respond to different therapeutic regimens in a dose-dependent and combination-dependent manner, as would be expected in real tumor tissues. Together, these assays were intended to evaluate whether the printed organoids could provide a quantitative readout for preliminary drug-response assessment.

As shown in Figure 6A, with increasing cisplatin concentration, the 3D structural integrity of the bioprinted organoids was progressively impaired, as reflected by loss of contour integrity, loosening of the architecture, and a

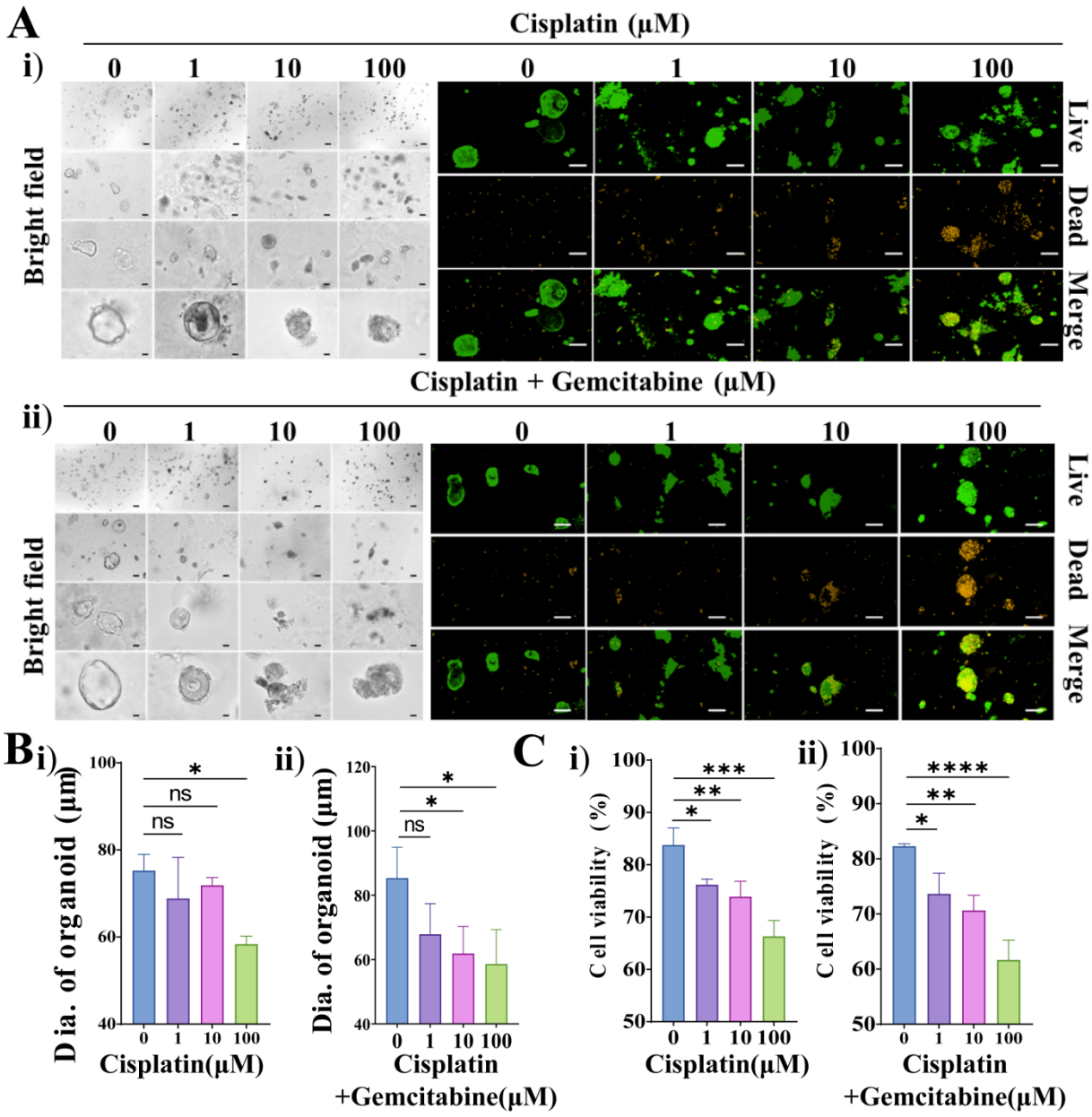

Figure 6. Drug sensitivity assessment of DLM–Ru/SPS:GelMA (4:1) hydrogel-based 3D bioprinted CCAO platform. The CCAO-laden hydrogel constructs were photocrosslinked under 405-nm light irradiation for 50 seconds. CCAO-1 organoids cultured in the 3D-printed bioink-based platform. (A) Representative bright-field and calcein-AM/PI live/Dead staining images of organoids cultured on the DLM–Ru/SPS:GelMA (4:1) hydrogel-based 3D bioprinted CCAO platform and treated with cisplatin alone (i) or cisplatin plus gemcitabine (ii) at concentrations of 0, 1, 10, and 100 μM after 72 hours of drug exposure. The Live/Dead staining images were obtained by confocal z-stack scanning and are shown as 2D projection images. For each treatment group, bright-field images are shown on the left, whereas live, dead, and merged fluorescence images are shown on the right. Scale bar: 100 μm. In calcein-AM/PI staining images, live cells are shown in green and dead cells in orange-yellow. (B) Quantitative analysis of organoid diameter following treatment with cisplatin alone (i) or cisplatin plus gemcitabine (ii) at different concentrations. Only organoids with diameters greater than 50 μm were included in the quantitative analysis. (C) Quantitative analysis of cell viability following treatment with cisplatin alone (i) or cisplatin plus gemcitabine (ii) at different concentrations. Data are presented as mean ± standard deviation. Statistical significance is indicated as follows: ns, not significant. Quantitative data are presented as mean ± standard deviation from $n = 3$ independent biological replicates unless otherwise indicated. Statistical significance is indicated as follows: ns, not significant; $^{*}p < 0.05$, $^{**}p < 0.01$, $^{***}p < 0.001$, $^{****}p < 0.0001$.

Abbreviations: 2D: Two-dimensional; 3D: Three-dimensional; CCAO: Cholangiocarcinoma organoid; DLM: Decellularized liver matrix; GelMA: Gelatin methacryloyl; PI: Propidium iodide; Ru: Ruthenium; SPS: Sodium persulfate.

reduction in the number of aggregates. In contrast to the morphologically uniform and well-defined spherical organoids described in the previous section, the drug-treated organoids clearly lost their compactness and structural integrity. This observation suggests that the 3D organoid structure was not only successfully established, but also sufficiently responsive to exogenous drug stimulation. Importantly, such structural responses are biologically meaningful, as the effects of anticancer drugs in native tumor tissues are often manifested not only through cell death, but also through disruption of the overall structural stability of the tumor mass. In this sense, the ability of a drug to perturb the spatial organization of the organoid constitutes an important component of its inhibitory effect. Therefore, the structural damage observed in Figure 6A indicates that the model exhibits a degree of tissue-level drug responsiveness, rather than merely single-cell cytotoxicity.

Further analysis of the Live/Dead staining results revealed that after cisplatin treatment, the AM-positive green fluorescence signal in the organoids gradually decreased, whereas the PI-positive orange-yellow fluorescence signal markedly increased, indicating a progressive rise in cell death with increasing drug concentration. Quantitative analysis also supported this trend, showing a dose-dependent decline in cell viability as cisplatin concentration increased (Figure 6A–6C). In parallel, the conventional Matrigel-cultured organoids exhibited a more pronounced decrease in viability only at the highest cisplatin concentration (100 μM) (Figure S11A), suggesting that matrix composition and the surrounding microenvironment may influence drug sensitivity in a concentration-dependent manner. This difference may be related to the regulatory effects of liver-specific ECM components. The native hepatic microenvironment is not a single matrix component but rather comprises multiple ECM molecules, including collagens, laminin, fibronectin, hyaluronic acid, and various proteoglycans, which collectively contribute to the maintenance of hepatocellular polarity, tissue organization, and signaling homeostasis. In contrast, Matrigel is primarily derived from basement membrane extracts and thus differs from the native liver microenvironment in both matrix composition and mechanical properties. These compositional differences may modulate cell–matrix adhesion, integrin-mediated signaling, and drug diffusion behavior, thereby affecting cisplatin accessibility within the organoids and the magnitude of cellular responses. Therefore, the enhanced reduction in viability observed in the Matrigel group at high cisplatin concentrations may not simply reflect intrinsic drug toxicity but may also indicate an important modulatory role of the matrix background in shaping drug-sensitivity phenotypes.

Notably, cisplatin sensitivity assays performed using two additional organoid lines, CCAO-2 and CCAO-3, showed that both lines were largely insensitive to low cisplatin concentrations (1 μM and 10 μM), while more evident viability loss was observed only at higher concentrations (Figure S11B and S11C). This suggests that there are clear sample-specific differences in cisplatin susceptibility, while the overall tendency toward increased response with rising drug concentration is still preserved. These findings further support the utility of this platform for capturing heterogeneous drug responses. This dose-dependent response was consistent with the aforementioned morphological observations and further confirmed the sensitivity of the printed organoids to chemotherapeutic stimulation at the functional level. More importantly, such a continuous response across low-to-high concentrations demonstrates the model's capacity for quantitative pharmacodynamic readout, which is essential for subsequent drug-screening applications. A truly useful drug sensitivity platform should not only distinguish between responsive and non-responsive states but also capture differences in drug effects across concentrations, thereby enabling more refined comparisons of efficacy and treatment optimization.

On this basis, we further evaluated the effects of combined cisplatin and gemcitabine treatment. Compared with cisplatin monotherapy, the combined treatment resulted in a further reduction in the viable cell signal and a pronounced increase in the dead cell signal within the organoids, suggesting that the combination regimen was more effective at disrupting the tumor-like structures and inducing cell death. Quantitative results showed that the reduction in cell viability in the combination group was significantly greater than that observed in the monotherapy group, indicating a stronger inhibitory effect of the two-drug regimen (Figure 6Aii, 6Bii, 6Cii and Figure S10B). More importantly, the differences in drug response were more evident under gemcitabine-cisplatin combination treatment, further highlighting the model's ability to capture treatment effects with greater clinical relevance and pharmacological discrimination. This finding is compatible with the known clinical use of gemcitabine–cisplatin chemotherapy in CCA and supports the feasibility of using this model for preliminary drug-response assessment. In other words, the organoids generated in this study did not lose drug sensitivity due to the bioprinting process but instead retained treatment responses consistent with those observed in clinical settings within a 3D microenvironment.

At a deeper level, these results indicate that the

"structural stability" and "biocompatibility" verified in the earlier sections are not merely independent material parameters, but fundamental prerequisites for subsequent pharmacological evaluation. Only when the organoids can form stably and maintain their 3D architecture over time can drugs exert their effects in a spatial context that more closely resembles the *in vivo* environment. Likewise, only when the bioink does not excessively interfere with cell viability can the observed pharmacological responses be interpreted as true drug effects rather than artifacts introduced by the material itself. Therefore, the results presented in Figure 6 constitute a functional validation of the material properties and organoid construction achieved in the preceding sections. They demonstrate that the optimized bioprinting system is not only suitable for constructing CCAOs but also capable of supporting subsequent drug-intervention experiments and faithfully recording drug-induced effects in tumor-like tissues.

In principle, 3D-printed organoids may offer advantages over conventional 2D culture for drug-sensitivity testing because they better preserve ECM encapsulation, spatial organization, and diffusion constraints. Cells cultured in 2D monolayers are typically exposed to a flat environment lacking ECM encapsulation, spatial polarity, and diffusion gradients, which often leads to more direct drug responses and may overestimate drug sensitivity. In contrast, cells in 3D organoids maintain closer spatial interactions, and drugs must penetrate the outer cell layers and overcome local barriers before affecting the inner regions, making their response patterns more representative of actual tumor tissues. The relatively stronger drug response observed in the Matrigel-based control may reflect differences in matrix stiffness, porosity, cell–matrix adhesion, or diffusional accessibility, all of which can alter the extent to which cisplatin reaches and affects the embedded cells. This is particularly relevant for CCA, a tumor type characterized by marked heterogeneity, for which 3D models are more likely to reflect differences in drug response among lesions, regions, and patients. Accordingly, Figure 6 not only demonstrates the direct cytotoxic effects of the drugs on the printed organoids but also indirectly highlights the capacity of this platform to mimic the *in vivo* tumor microenvironment.

In summary, the successfully established 3D CCAO model exhibited a clear dose-dependent response to cisplatin, with cell viability progressively decreasing as the drug concentration increased. In addition, combined treatment with cisplatin and gemcitabine produced a more pronounced reduction in viable cells and a corresponding increase in dead cells, indicating a stronger antitumor effect than cisplatin alone. Although the Matrigel-based control showed a somewhat greater apparent sensitivity at high cisplatin concentration, the bioprinted organoids still maintained clear and reproducible drug responses across different treatment conditions, supporting the reliability of the DLM–Ru/SPS:GelMA bioink platform for 3D drug evaluation. These results demonstrate that the DLM–Ru/SPS:GelMA bioink not only facilitates organoid formation and phenotype maintenance, but also provides a robust 3D system for preliminary chemotherapeutic assessment. Accordingly, this model holds considerable promise for CCA drug screening, combination therapy evaluation, and precision medicine research.

Although this study successfully established a 3D bioprinted CCAO model using the DLM–Ru/SPS:GelMA bioink and demonstrated its potential for structural maintenance, biocompatibility, and drug-response evaluation, several limitations remain. First, the current study was validated using a relatively limited number of CCA samples, and further investigations with a larger cohort of patient-derived specimens are needed to confirm the robustness and generalizability of this platform. Second, the present model primarily focuses on tumor cells and matrix support structures, while key components of the native tumor microenvironment, such as immune cells, vascular networks, and other stromal elements, have not yet been fully recapitulated. As a result, its physiological complexity still requires further improvement. In addition, this study mainly evaluated short-term responses to cisplatin and gemcitabine, whereas future studies should expand to additional chemotherapeutic agents, targeted therapies, and long-term treatment strategies to further explore drug resistance mechanisms and individualized drug screening. With the further incorporation of multicellular co-culture systems and clinically derived patient samples, this bioprinted organoid platform may provide greater translational value for precision medicine and drug development in CCA.

4. Conclusion

In this study, we developed a 3D bioprinted CCAO model using the optimized DLM–Ru/SPS:GelMA bioink. The printed organoids exhibited stable spherical morphology, high cell viability, and sustained expression of cholangiocyte-related markers, demonstrating the capability of this bioink system to support both structural formation and functional maintenance of CCAOs. Moreover, the model showed a clear dose-dependent response to cisplatin, and combined cisplatin–gemcitabine treatment produced a significantly stronger inhibitory effect, indicating that the platform can recapitulate clinically relevant chemotherapeutic responses. These

findings suggest that the bioprinted organoid model is a promising proof-of-concept tool for tumor modeling and drug-sensitivity testing in CCA, although further validation in larger patient cohorts and longer-term culture systems is required before clinical translation.

Acknowledgments

None.

Funding

This work was supported by the National Natural Science Foundation of China (grant no. 82272188), the National Key Research and Development Program of China (grant no. 2022YFA1105200), the Sichuan Central Guided Local Science and Technology Development Special Project (grant no. 2025ZYD0012), the Science and Technology Program of Sichuan Province (grant no. 2025JDRC0057), the "Jie Bang Gua Shuai" Science and Technology Project of Chengdu (grant no. 2024-JB00-00018-GX), and the Strategic Research Bureau of Chengdu Eastern New Area (grant no. 2024-DBXQ-KJYF002).

Conflict of interest

The authors declare they have no competing interests.

Author contributions

Conceptualization: Qiumei Yan, Wenqi Hu, Guohua Wu, Xiongwen Chen, Bangchuan Hu

Formal analysis: Di Wu, Qijun Du, Luping Lü, Zhuge Yang, Jiashu Wang

Investigation: Qiumei Yan, Wenqi Hu, Jiashu Wang

Methodology: Qiumei Yan, Wenqi Hu, Jiashu Wang, Luping Lü, Zhuge Yang

Writing–original draft: Qiumei Yan, Zixuan Pan, Yonggang Guo, Jie Liu, Huanhuan Chen

Writing–review & editing: Haijie Hu, Bin Lai, Yabao Liu, Guohua Wu, Xiongwen Chen, Bangchuan Hu

Ethics approval and consent to participate

CCA tissues were obtained from patients who underwent surgical resection. In total, three patient-derived CCA organoid lines were established. The study protocol was approved by the Biomedical Ethics Committee of West China Hospital, Sichuan University (2023-108), and was conducted in accordance with the Declaration of Helsinki. Written informed consent was obtained from all patients for the collection and use of their tissue samples for research purposes. Normal porcine liver tissues were obtained from a local commercial market in Chengdu, China, as by-products of the food industry and therefore did not require animal ethics approval.

Consent for publication

Not applicable.

Availability of data

The raw data supporting the findings of this study are available from the corresponding author upon reasonable request.

References

1. Li Z, Zhou H, Xia Z, *et al.* HMGA1 augments palbociclib efficacy via PI3K/mTOR signaling in intrahepatic cholangiocarcinoma. *Biomark Res.* 2023;11(1):33.

   doi: 10.1186/s40364-023-00473-w

2. Cao H, Huang T, Dai M, *et al.* Tumor Microenvironment and its Implications for Antitumor Immunity in Cholangiocarcinoma: Future Perspectives for Novel Therapies. *Int J Biol Sci.* 2022;18(14):5369-5390.

   doi: 10.7150/ijbs.73949

3. Ilyas SI, Affo S, Goyal L, *et al.* Cholangiocarcinoma - novel biological insights and therapeutic strategies. *Nat Rev Clin Oncol.* 2023;20(7):470-486.

   doi: 10.1038/s41571-023-00770-1

4. Serra-Camprubi Q, Verdaguer H, Oliveros W, *et al.* Human Metastatic Cholangiocarcinoma Patient-Derived Xenografts and Tumoroids for Preclinical Drug Evaluation. *Clin Cancer Res.* 2023;29(2):432-445.

   doi: 10.1158/1078-0432.CCR-22-2551

5. Wabitsch S, Tandon M, Ruf B, *et al.* Anti-PD-1 in Combination With Trametinib Suppresses Tumor Growth and Improves Survival of Intrahepatic Cholangiocarcinoma in Mice. *Cell Mol Gastroenterol Hepatol.* 2021;12(3):1166-1178.

   doi: 10.1016/j.jcmgh.2021.05.011

6. Lapitz A, Azkargorta M, Milkiewicz P, *et al.* Liquid biopsy-based protein biomarkers for risk prediction, early diagnosis, and prognostication of cholangiocarcinoma. *J Hepatol.* 2023;79(1):93-108.

   doi: 10.1016/j.jhep.2023.02.027

7. Cadamuro M, Al-Taee AGonda TA. Advanced endoscopy meets molecular diagnosis of cholangiocarcinoma. *J Hepatol.* 2023;78(5):1063-1072.

   doi: 10.1016/j.jhep.2023.01.027

8. Zhang N, Sun L, Zhou S, *et al.* Cholangiocarcinoma PDHA1

succinylation suppresses macrophage antigen presentation via alpha-ketoglutaric acid accumulation. *Nat Commun.* 2025;16(1):3177.

doi: 10.1038/s41467-025-58429-7

9. Lin YY, Kuo HH, He ZJ, *et al.* SLC25A11-mediated reprogramming of mitochondrial redox state and lipid peroxidation confers NRF2-dependent ferroptosis resistance in biliary tract cancer. *Cell Mol Biol Lett.* 2026;31(1).

doi: 10.1186/s11658-025-00843-2

10. Liu C, Wang X, Liu E, *et al.* Deciphering cholangiocarcinoma heterogeneity and specific progenitor cell niche of extrahepatic cholangiocarcinoma at single-cell resolution. *J Hematol Oncol.* 2025;18(1):66.

doi: 10.1186/s13045-025-01716-z

11. Feng Y, Zhao M, Wang L, *et al.* The heterogeneity of signaling pathways and drug responses in intrahepatic cholangiocarcinoma with distinct genetic mutations. *Cell Death Dis.* 2024;15(1):34.

doi: 10.1038/s41419-023-06406-7

12. Li S, Yang K, Chen X, *et al.* Simultaneous 2D and 3D cell culture array for multicellular geometry, drug discovery and tumor microenvironment reconstruction. *Biofabrication.* 2021;13(4).

doi: 10.1088/1758-5090/ac1ea8

13. Abuwatfa WH, Pitt WGHusseini GA. Scaffold-based 3D cell culture models in cancer research. *J Biomed Sci.* 2024;31(1):7.

doi: 10.1186/s12929-024-00994-y

14. Barozzi DScielzo C. Emerging Strategies in 3D Culture Models for Hematological Cancers. *Hemasphere.* 2023;7(8):e932.

doi: 10.1097/HS9.0000000000000932

15. Xiang H, Chen F, Dong Z, *et al.* A microfluidic tumor-on-chip platform deciphers hypoxia-driven FOXO3a/PD-L1 signaling in gastric cancer immunotherapy resistance. *Mater Today Bio.* 2025;33:101925.

doi: 10.1016/j.mtbio.2025.101925

16. Qiao L, Yang G, Deng T, *et al.* Prophylactic supplementation with biogenic selenium nanoparticles mitigated intestinal barrier oxidative damage through suppressing epithelial-immune crosstalk with gut-on-a-chip. *J Adv Res.* 2026;80:197-218.

doi: 10.1016/j.jare.2025.04.023

17. Nguyen OTP, Misun PM, Hierlemann ALohasz C. A Versatile Intestine-on-Chip System for Deciphering the Immunopathogenesis of Inflammatory Bowel Disease. *Adv Healthc Mater.* 2024;13(7):e2302454.

doi: 10.1002/adhm.202302454

18. Zheng M, Qu J, Xiang DXing L. Organoids in lung cancer brain metastasis: Foundational research, clinical translation, and prospective outlooks. *Biochim Biophys Acta Rev Cancer.* 2025;1880(1):189235.

doi: 10.1016/j.bbcan.2024.189235

19. Li Z, Fu C, Chen Y, *et al.* D-amino acid oxidase suppresses hepatocellular carcinoma via oxidizing D-amino acids. *J Transl Med.* 2025;23(1):1359.

doi: 10.1186/s12967-025-07399-x

20. Di Carlo E. Tumor-on-chip's alliance with molecular pathology against metastatic disease. *J Biomed Sci.* 2026;33(1):9.

doi: 10.1186/s12929-025-01209-8

21. Lu Y, Du L, Sun M, *et al.* Patient-Derived 3D-Bioprinted Intrahepatic Cholangiocarcinoma Models Recapitulate Tumor Autologous Traits and Predict Personalized Adjuvant Therapy. *Adv Sci.* 2026;13(22):e22025.

doi: 10.1002/advs.202522025

22. Zhang X, Jiang W, Wu X, *et al.* Divide-and-conquer strategy with engineered ossification center organoids for rapid bone healing through developmental cell recruitment. *Nat Commun.* 2025;16(1):6200.

doi: 10.1038/s41467-025-61619-y

23. Habib MAKhoda B. Rheological Analysis of Bio-ink for 3D Bio-printing Processes. *J Manuf Process.* 2022;76:708-718.

doi: 10.1016/j.jmapro.2022.02.048

24. Debnath S, Agrawal A, Jain N, Chatterjee KPlayer DJ. Collagen as a bio-ink for 3D printing: a critical review. *J Mater Chem B.* 2025;13(6):1890-1919.

doi: 10.1039/d4tb01060d

25. Kozlowski MT, Crook CJKu HT. Towards organoid culture without Matrigel. *Commun Biol.* 2021;4(1):1387.

doi: 10.1038/s42003-021-02910-8

26. Zhu L, Yuhan J, Yu H, Zhang B, Huang KZhu L. Decellularized Extracellular Matrix for Remodeling Bioengineering Organoid's Microenvironment. *Small.* 2023;19(25):e2207752.

doi: 10.1002/smll.202207752

27. Gan Z, Qin X, Liu H, Liu JQin J. Recent advances in defined hydrogels in organoid research. *Bioact Mater.* 2023;28:386-401.

doi: 10.1016/j.bioactmat.2023.06.004

28. Guo X, Liu B, Zhang Y, *et al.* Decellularized extracellular matrix for organoid and engineered organ culture. *J Tissue Eng.* 2024;15:20417314241300386.

doi: 10.1177/20417314241300386

29. Perin F, Ouyang L, Lim KS, *et al.* Bioprinted Constructs in the Regulatory Landscape: Current State and Future

Perspectives. *Adv Mater.* 2026;38(4):e04037.

doi: 10.1002/adma.202504037

30. Xu P, Kankala RK, Wang SChen A. Decellularized extracellular matrix-based composite scaffolds for tissue engineering and regenerative medicine. *Regen Biomater.* 2024;11:rbad107.

doi: 10.1093/rb/rbad107

31. Willemse J, van Tienderen G, van Hengel E, *et al.* Hydrogels derived from decellularized liver tissue support the growth and differentiation of cholangiocyte organoids. *Biomaterials.* 2022;284:121473.

doi: 10.1016/j.biomaterials.2022.121473

32. Tabatabaei Rezaei N, Kumar H, Liu H, *et al.* Bioprinting of hepatic tissue model using photocrosslinkable dECM-containing composite hydrogel. *Mater Today Bio.* 2025;32:101824.

doi: 10.1016/j.mtbio.2025.101824

33. Fang W, Yang M, Wang L, *et al.* Hydrogels for 3D bioprinting in tissue engineering and regenerative medicine: Current progress and challenges. *Int J Bioprint.* 2023;9(5):759.

doi: 10.18063/ijb.759

34. Musah SArzaghi H. Unleashing the power of biomaterials to enhance organoid differentiation and function. *Nat Methods.* 2024;21(9):1575-1577.

doi: 10.1038/s41592-024-02393-5

35. Liu S, Chen G, Chen Z, Wang FLv Y. Research progress on stiffness controllable scaffolds based on gelatin methacryloyl hydrogels for tissue repair and reconstruction. *Int J Biol Macromol.* 2025;321:146485.

doi: 10.1016/j.ijbiomac.2025.146485

36. Zhou M, Lee BH, Tan YJTan LP. Microbial transglutaminase induced controlled crosslinking of gelatin methacryloyl to tailor rheological properties for 3D printing. *Biofabrication.* 2019;11(2):025011.

doi: 10.1088/1758-5090/ab063f

37. Hu W, Bei HP, Jiang H, *et al.* DLM-GelMA/tumor slice sandwich structured tumor on a chip for drug efficacy testing. *Lab Chip.* 2024;24(15):3718-3727.

doi: 10.1039/d4lc00278d

38. Wu L, Wu G, Wu D, *et al.* Stiffness-Tunable Hydrogel Microfluidic Chip Reveals the Role of Stiffness in Cholangiocarcinoma Invasion and Pre-Metastatic Niche Formation. *Adv Healthc Mater.* 2026;15(9):e03515.

doi: 10.1002/adhm.202503515

39. Zhou B, Jiang X, Zhou X, *et al.* GelMA-based bioactive hydrogel scaffolds with multiple bone defect repair functions: therapeutic strategies and recent advances. *Biomater Res.* 2023;27(1):86.

doi: 10.1186/s40824-023-00422-6

40. Smits J, van der Pol A, Goumans MJ, Bouten CVCJorba I. GelMA hydrogel dual photo-crosslinking to dynamically modulate ECM stiffness. *Front Bioeng Biotechnol.* 2024;12:1363525.

doi: 10.3389/fbioe.2024.1363525

41. Crapo PM, Gilbert TWBadylak SF. An overview of tissue and whole organ decellularization processes. *Biomaterials.* 2011;32(12):3233-3243.

doi: 10.1016/j.biomaterials.2011.01.057

42. Pati F, Jang J, Ha DH, *et al.* Printing three-dimensional tissue analogues with decellularized extracellular matrix bioink. *Nat Commun.* 2014;5(1):3935.

doi: 10.1038/ncomms4935

43. Mao Q, Wang Y, Li Y, *et al.* Fabrication of liver microtissue with liver decellularized extracellular matrix (dECM) bioink by digital light processing (DLP) bioprinting. *Mater Sci Eng C.* 2020;109:110625.

doi: 10.1016/j.msec.2020.110625

44. Yu C, Ma X, Zhu W, *et al.* Scanningless and continuous 3D bioprinting of human tissues with decellularized extracellular matrix. *Biomaterials.* 2019;194:1-13.

doi: 10.1016/j.biomaterials.2018.12.009

45. Lim KS, Klotz BJ, Lindberg GCJ, *et al.* Visible Light Cross-Linking of Gelatin Hydrogels Offers an Enhanced Cell Microenvironment with Improved Light Penetration Depth. *Macromol Biosci.* 2019;19(6):e1900098.

doi: 10.1002/mabi.201900098